E-plane waveguide filtering six-port junction

Chen, Xun; Wang, Yi; Skaik, Talal; Zhang, Qingfeng

DOI:
10.1109/TMTT.2021.3120094

Document Version
Peer reviewed version

Citation for published version (Harvard):
Chen, X, Wang, Y, Skaik, T & Zhang, Q 2021, 'E-plane waveguide filtering six-port junction', *IEEE Transactions on Microwave Theory and Techniques*, vol. 69, no. 12, pp. 5360-5370.
https://doi.org/10.1109/TMTT.2021.3120094

E-Plane Waveguide Filtering Six-Port Junction

Xun Chen, Yi Wang, *Senior Member IEEE,* Talal Skaik and Qingfeng Zhang, *Senior Member IEEE*

***Abstract*— A novel E-plane filtering six-port junction (SPJ) based on waveguide is presented. Different from the traditional designs, the proposed SPJ is formed by two identical filtering 180° couplers and two waveguide couplers with 180° and 90° phase shifts. A coupling-matrix (CM) technique, combining both resonant and non-resonant structures, has been developed to represent the entire SPJ. This has been used to predict the theoretical response as well as to investigate the effect of the couplers on the performance of the SPJ. A demonstrator has been designed to work at 10 GHz with a bandwidth of 0.4 GHz. Stub-loaded waveguide resonators have been used to keep a consistent profile and ease the layout of the complicated waveguide network. A good agreement between the CM-based theoretical responses, simulations and measurement has been achieved. The measured average insertion loss is 0.4 dB and the maximum in-band phase error is 10°. The measured in-band isolation between two input ports is higher than 26 dB.**

***Index Terms*— coupling matrix, filtering coupler, six-port junction, waveguide**

I. Introduction

SIX-PORT JUNCTIONS (SPJs), used in six-port receivers [1] or six-port reflectometers (SPRs) [2], are passive devices that were first reported in power-measuring devices [3] by Engen and Hoer. In 1994, the six-port concept was first introduced to communication systems [4]. An SPJ has two inputs and four outputs. It combines the two input signals in four different phase configurations at the four outputs with a 90° increment. Together with power detectors, SPJs can be used to replace mixers in receivers [5]. They generally have high power capacity and can work at high frequency domain (above 100 GHz) [5]. Many SPJs have been reported in different configurations. A multi-layer-structure based SPJ was reported in [6]. It has three couplers and one power divider. Because of the multi-layer structure, the size of the SPJ was reduced by about 78% compared to a planar design. In [7], substrate integrated waveguide (SIW) was used in the design of SPJ. Different from [6], it contains two hybrid couplers, two power dividers and two phase shifters. With the same configuration, [8] demonstrated a SPJ with polarization-selective coupling, which allows the application of polarization-inclusive remote sensing.

With the rapid development of radio-frequency (RF) front ends, the number of cascaded functional devices is increasing. This leads to the increase in the overall size, power losses and noise. Filters may be used at various locations along the RF chain either for signal selection or interference/harmonics rejection and they are often one of the largest components. Embedding filtering functions in other passive components, without cascading separate filters, offers added functionality without adversely increasing the footprint of passive devices. Such integration techniques have drawn more and more attention. New circuit structures have been demonstrated, such as filtering antennas [9], filtering couplers [10] and filtering Butler matrices [11] to name just a few. The benefit of the integration technique is particularly noteworthy for multi-port signal distribution networks because the space occupied by multiple filters could be saved [11] by merging and embedding these into the network. Similar benefit is foreseeable for SPJs as the one shown in [12]. The four filters at the output ports could be absorbed by the SPJ itself. This paper proposes a prototype design demonstrating this concept. The work also formulates a coupling-matrix based analytical approach to treat a complex multi-port network with both resonant and non-resonant structures as a whole.

We only identified one paper [13] that mentioned the application of a filtering coupler in a filtering SPJ. However, it did not illustrate the detail of the design. This work details the design of an E-plane waveguide filtering SPJ working at 10 GHz. The proposed SPJ consists of two identical filtering couplers and two E-plane waveguide couplers with 180° and

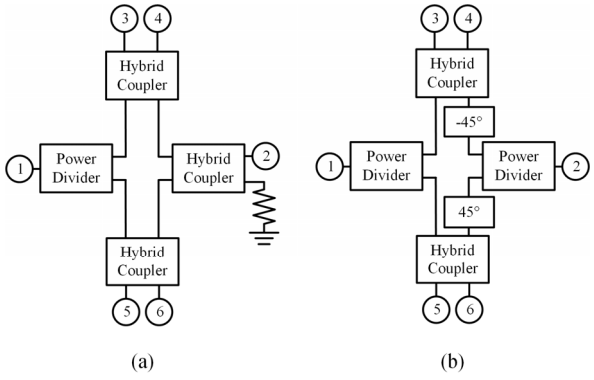

Fig. 1. Two typical topologies of conventional SPJs. (a) Three hybrid couplers and one power divider. (b) Two hybrid couplers and two power dividers. The hybrids are all 90° couplers.

The work was supported by the U.K. Engineering and Physical Science Research Council (EPSRC) under Contract EP/S013113/1 and supported in part by the National Natural Science Foundation of China under Grant 61871207 and in part by the Shenzhen Science and Technology Innovation Committee Funds under Grant JCYJ20190809115419425. (Corresponding author: Yi Wang and Qingfeng Zhang.)

X. Chen and Q. Zhang are with the Department of Electronics and Electrical Engineering, Southern University of Science and Technology, Shenzhen 518055, China. X. Chen is also with the University of Birmingham, U.K. (e-mail: zhang.qf@sustech.edu.cn).

T. Skaik and Yi Wang are with the School of Engineering, The University of Birmingham, Birmingham B15 2TT, U.K. (e-mail: Y.Wang.1@bham.ac.uk).

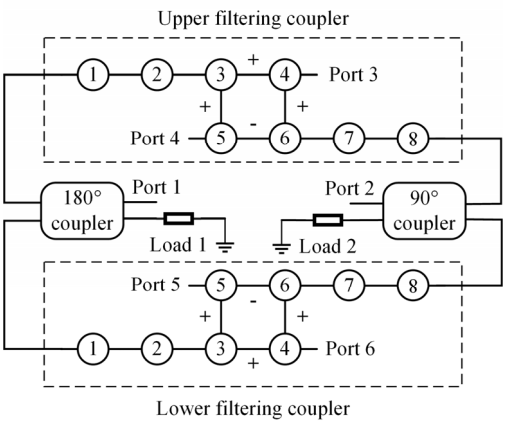

Fig. 2. Schematic of the fourth-order filtering SPJ. The upper and lower structures are identical fourth-order filtering couplers.

90° phase shifts, respectively. The E-plane filtering couplers were designed with a fourth-order Chebyshev response. To analyze the response of the SPJ as a whole, a coupling matrix (CM) combining the two filtering couplers and two non-resonant couplers was constructed. This is achieved by a method that transfers the Y-matrices of non-resonant components to the couplings in the CM. The combined CM not only can be used in the prediction of the ideal response of the SPJ, but also can be applied in the cases where the responses of the non-resonant structures are already determined. The E-plane-cut configuration was employed to minimize the losses at the cutting plane. Furthermore, to ease the layout of the filtering couplers, two symmetrical stubs are featured in each resonator. The depths of the stub-pairs are used to control the resonant frequencies without changing the outer dimensions. An SPJ working at 10 GHz, with a bandwidth of 400 MHz, is chosen as a prototype to demonstrate the device topology and the CM method. This technique may be applied to higher millimeter-wave frequencies.

This paper is organised as follows. The topology of the SPJ will be explained in Section II. In Section III, the CM underpinning the filtering SPJ will be given and the theoretical analysis method will be presented. This is followed with the detailed designs of the waveguide couplers and the application of the hybrid CM to predict the response of the SPJ in Section IV. The design of the filtering coupler is given in Section V. Section VI presents the use of the CM fabricated SPJ and its measurement results.

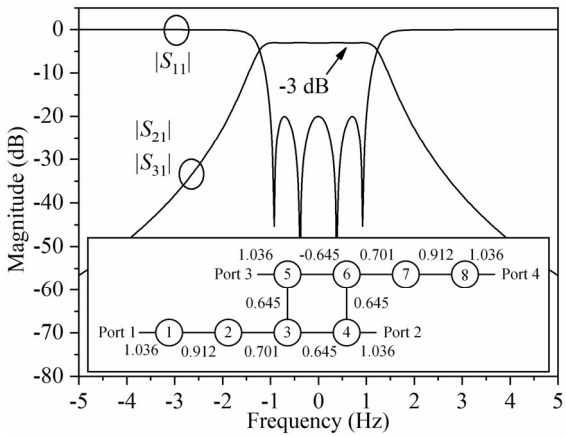

Fig. 3. Theoretical magnitude response of the fourth-order filtering coupler based on the synthesized CM, values of which are given in the inset.

II. SPJ Topology

Two typical topologies of the conventional non-filtering SPJs are illustrated in Fig. 1. Fig. 1(a) is an SPJ consisting of three 90° hybrid couplers and one power divider. One of the couplers has one port loaded. The other topology, shown in Fig. 1(b), replaces one hybrid coupler with a power divider. All the couplers in the two topologies are 3-dB 90° couplers. Two phase shifters with opposite phase shift may be needed in the topology in Fig. 1(b).

The proposed filtering SPJ is composed of two filtering couplers and two waveguide couplers, as illustrated in Fig. 2. Port 1 and Port 2 are the two inputs while Port 3-6 are the four outputs. Different from the conventional SPJ topologies, the upper and lower couplers in the proposed SPJ are 180° filtering couplers (rather than 90° hybrids) with eight resonators in each. The coupler on the left is a 180° 3-dB coupler and its outputs have a 180° phase difference when the input is at Port 1. The coupler on the right is a 90° 3-dB coupler and its outputs have a 90° phase difference when the input signal is at Port 2. When an input signal goes into resonator 1 of the upper coupler or similarly the lower coupler, it is equally divided with no phase shift between the output Ports 3 and 4 of the upper coupler or the Ports 5 and 6 of the lower coupler. However, when an input signal goes into resonator 8 of either of the filtering couplers, it will be split in half with 180° phase shift between Port 3 and 4 of the upper coupler, and similarly between Port 5 and 6 for the lower coupler. Furthermore, when two input signals are applied at Port 1 and Port 2, the phase differences at the four output ports will be (all the negative values have been added 360° to make them positive):

$$\begin{cases} \angle S_{31} - \angle S_{32} = 0^\circ \\ \angle S_{41} - \angle S_{42} = 180^\circ \\ \angle S_{51} - \angle S_{52} = 90^\circ \\ \angle S_{61} - \angle S_{62} = 270^\circ \end{cases} \quad (1)$$

The two 180° filtering couplers are identical. They are designed to have a fourth-order Chebyshev response with an in-band $|S_{11}|_{\max}$ of -20 dB. Its coupling topology is shown in the inset of Fig. 3 with the corresponding theoretical response. The circles represent the resonators whereas the lines between them indicate the coupling, m_{ij} (i and j are the indices of the resonators). The CM of the four-port coupler, which contains all the inter-resonator couplings, can be reduced to its two-port equivalent for its symmetry. Therefore, the CM of the coupler can be synthesized using established methods [14]. Port 1 and 4 are isolated from each other. This is realized by the opposite couplings ($m_{56} = -m_{46} = -0.645$). Note $|S_{41}|$ is zero ideally ($-\infty$ in dB).

III. CM Representation of the SPJ

Coupling matrices are widely used in the synthesis of

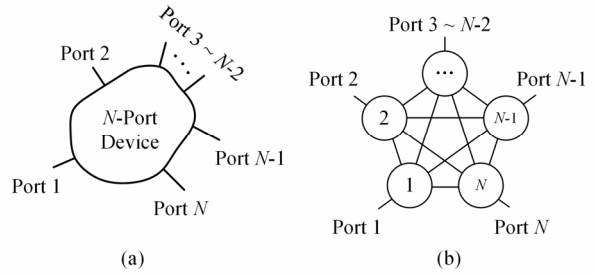

Fig. 4. (a) Diagrammatic representation of a non-resonant *N*-port device. (b) *N*-port non-resonant device represented by an *N*-port *N*-node network.

filters and other resonant circuits. For circuits involving both resonant and non-resonant components, the traditional design approach often treat the components separately and connect them through matching circuits [15], [16]. This 'cascaded' approach cannot easily and accurately predict the theoretical responses of a complicated circuit network. Practically it also introduces additional losses associated with the interconnection. To circumvent this problem, the CM technology has been extended to more generic forms to include transmission lines and even active devices [17] - [19]. By doing so, the theoretical response of many circuits (no longer limited to filters) can be predicted using a generic or active CM. The CM can also be used for circuit synthesis and optimization. In the proposed topology of the SPJ shown in Fig. 2, there are two waveguide couplers. Since they are not resonant structures, it is not straightforward to include them in a CM for the whole SPJ. A method, extended from [17], will be given in this section, to weave the Y-matrices of the two non-resonant couplers into the CM of the SPJ. This CM can be used for further optimization as a whole. Or, part of the matrix may be usefully populated by values representing simulated sub-circuits, whereas the rest of the matrix may be synthesized accordingly.

Fig. 4(a) illustrates a generic non-resonant *N*-port device. Assume the *Y*-parameters of the device are Y_{ij} (i, j = 1…N). In order to derive the CM of this non-resonant device, *J*-inverters [20] are added to the ports. The device is redrawn in Fig. 5. There is an input current from Port 1, namely i_s. $Y_{P,k}$ (k = 1 to N) are the port admittances. $v_{P,k}$ (k = 1 to N) and v_k (k = 1 to N) are to depict the node voltages for the ports and the device

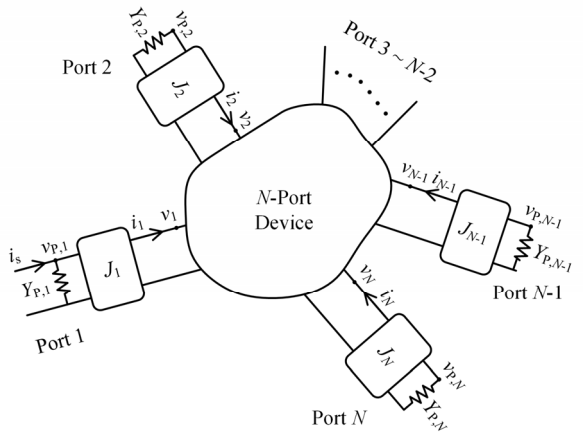

Fig. 5. *N*-port device with *J*-inverters at the ports.

respectively while i_k (k = 1 to N) are the currents to the device. Applying Kirchoff's current law at each node of the circuit in Fig. 5, the relationship between the current and voltage can be written by:

$$\begin{cases} Y_{P,1}v_{P,1} - jJ_1v_1 = i_s \\ -jJ_1v_{P,1} + Y_{1,1}v_1 + Y_{1,2}v_2 + \cdots + Y_{1,N}v_N = 0 \\ Y_{P,2}v_{P,2} - jJ_2v_2 = 0 \\ -jJ_2v_{P,2} + Y_{2,1}v_1 + Y_{2,2}v_2 + \cdots + Y_{2,N}v_N = 0 \\ \vdots \\ Y_{P,N-1}v_{P,N-1} - jJ_{N-1}v_{N-1} = 0 \\ -jJ_{N-1}v_{P,N-1} + Y_{N-1,1}v_1 + Y_{N-1,2}v_2 + \cdots + Y_{N-1,N}v_N = 0 \\ Y_{P,N}v_{P,N} - jJ_Nv_N = 0 \\ -jJ_Nv_{P,N} + Y_{N,1}v_1 + Y_{N,2}v_2 + \cdots + Y_{N,N}v_N = 0 \end{cases} \tag{2}$$

In applying the CM method to non-resonant structures, the values of *J*-inverters are set to be 1, which means the circuits on both sides are connected directly. The admittances of the ports in this device are also normalized to 1 for perfect match, (2) can be re-arranged to:

$$\begin{bmatrix} Y_{1,1} & Y_{1,2} & \cdots & Y_{1,N} & -j & 0 & \cdots & 0 \\ Y_{2,1} & Y_{2,2} & \cdots & Y_{2,N} & 0 & -j & \cdots & 0 \\ \vdots & \vdots & \vdots & \vdots & \vdots & \vdots & \vdots & \vdots \\ Y_{N,1} & Y_{N,2} & \cdots & Y_{N,N} & 0 & 0 & \cdots & -j \\ -j & 0 & \cdots & 0 & 1 & 0 & \cdots & 0 \\ 0 & -j & \cdots & 0 & 0 & 1 & \cdots & 0 \\ \vdots & \vdots & \vdots & \vdots & \vdots & \vdots & \vdots & \vdots \\ 0 & 0 & \cdots & -j & 0 & 0 & \cdots & 1 \end{bmatrix} \begin{bmatrix} v_1 \\ v_2 \\ \vdots \\ v_N \\ v_{P,1} \\ v_{P,2} \\ \vdots \\ v_{P,N} \end{bmatrix} = \begin{bmatrix} 0 \\ 0 \\ \vdots \\ 0 \\ i_s \\ 0 \\ \vdots \\ 0 \end{bmatrix} \tag{3}$$

Following the same steps as in [17], (3) can be finally simplified to:

$$[A][v] = [i] \tag{4}$$

where $[A]$ is a $2N \times 2N$ matrix and it consists of:

$$[A] = [x] + [u] - j[m] \tag{5}$$

$[x]$ is a diagonal matrix with entries of $\{Y_{1,1}, Y_{2,2}, \ldots, Y_{N,N}, 1,1, \ldots, 1\}$ (N sets of 1) and $[u]$ is a diagonal matrix representing the resonant nodes. $[u]$ is 0 in this case. $[m]$ is a $2N \times 2N$ CM of the *N*-port non-resonant structure, which is:

$$[m] = \begin{bmatrix} 0 & jY_{1,2} & \cdots & jY_{1,N} & 1 & 0 & \cdots & 0 \\ jY_{2,1} & 0 & \cdots & jY_{2,N} & 0 & 1 & \cdots & 0 \\ \vdots & \vdots & \vdots & \vdots & \vdots & \vdots & \vdots & \vdots \\ jY_{N,1} & jY_{N,2} & \cdots & 0 & 0 & 0 & \cdots & 1 \\ 1 & 0 & \cdots & 0 & 0 & 0 & \cdots & 0 \\ 0 & 1 & \cdots & 0 & 0 & 0 & \cdots & 0 \\ \vdots & \vdots & \vdots & \vdots & \vdots & \vdots & \vdots & \vdots \\ 0 & 0 & \cdots & 1 & 0 & 0 & \cdots & 0 \end{bmatrix} \tag{6}$$

From (6), the *N*-port non-resonant device shown in Fig. 5 can be regarded as an *N*-port *N*-node structure, shown in Fig. 4(b). The coupling values between the nodes are $jY_{j,k}$ (j, k = 1 to N, $j \neq k$), and all the external quality factors are 1.

The above presents a generic method to obtain the CM for a non-resonant device based on the *Y*-matrix. In order to get the

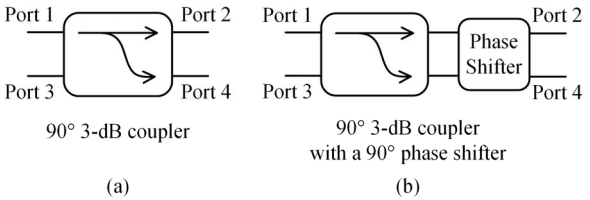

Fig. 6. Two hybrid couplers. (a) a 90° 3-dB coupler. (b) a 180° coupler formed of a 90° 3-dB coupler with a 90° phase shifter. Note here the phase shifter is a four-port device with a reference line.

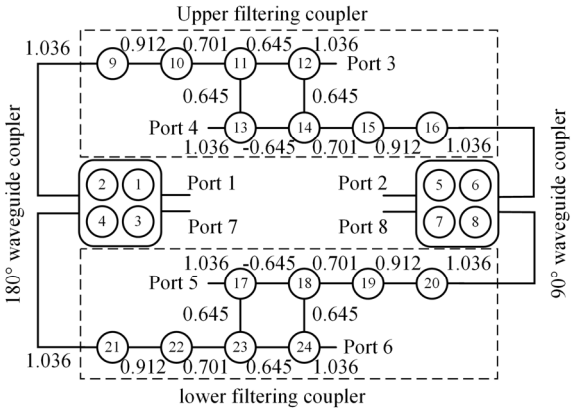

Fig. 7. Topology of the SPJ when transformed into nodes.

CM of the SPJ, the CMs of the two waveguide couplers (as non-resonant devices) need to be constructed first using the above method. The 90° hybrid coupler used in the SPJ is the conventional and the 180° hybrid coupler is formed by a conventional 90° hybrid coupler and a 90° phase shifter (includes one reference line). Both are shown in Fig. 6. Note that, for both couplers, Port 1 is the input, Port 2 and Port 4 are outputs and Port 3 is the isolated port. Interconnection lines are inevitable between the waveguide couplers and the filtering couplers. To represent these lines, an initial phase θ is added to each port. The *S*-parameters of the 90° hybrid coupler are given by [21]:

$$[S_{90}] = -\frac{1}{\sqrt{2}}\begin{bmatrix} 0 & e^{j(\pi/2+\theta)} & 0 & e^{j\theta} \\ e^{j(\pi/2+\theta)} & 0 & e^{j\theta} & 0 \\ 0 & e^{j\theta} & 0 & e^{j(\pi/2+\theta)} \\ e^{j\theta} & 0 & e^{j(\pi/2+\theta)} & 0 \end{bmatrix} \quad (7)$$

By adding a 90° phase shifter to Port 4 (a reference line to Port 2), a 180° hybrid coupler is formed. Its *S*-parameters are:

$$[S_{180}] = -\frac{1}{\sqrt{2}}\begin{bmatrix} 0 & e^{j(\pi/2+\theta)} & 0 & e^{j(-\pi/2+\theta)} \\ e^{j(\pi/2+\theta)} & 0 & e^{j\theta} & 0 \\ 0 & e^{j\theta} & 0 & e^{j\theta} \\ e^{j(-\pi/2+\theta)} & 0 & e^{j\theta} & 0 \end{bmatrix} \quad (8)$$

Now convert the two *S*-parameter matrices into *Y*-matrices [21]:

$$[Y_{90}] = j\sec 2\theta\begin{bmatrix} -\sin 2\theta & \sqrt{2}\cos\theta & 1 & -\sqrt{2}\sin\theta \\ \sqrt{2}\cos\theta & -\sin 2\theta & -\sqrt{2}\sin\theta & 1 \\ 1 & -\sqrt{2}\sin\theta & -\sin 2\theta & \sqrt{2}\cos\theta \\ -\sqrt{2}\sin\theta & 1 & \sqrt{2}\cos\theta & -\sin 2\theta \end{bmatrix} \quad (9)$$

$$[Y_{180}] = j\begin{bmatrix} -\tan\theta & \frac{\sec\theta}{\sqrt{2}} & 0 & -\frac{\sec\theta}{\sqrt{2}} \\ \frac{\sec\theta}{\sqrt{2}} & \cot 2\theta & \frac{\csc\theta}{\sqrt{2}} & \csc 2\theta \\ 0 & \frac{\csc\theta}{\sqrt{2}} & \cot\theta & \frac{\csc\theta}{\sqrt{2}} \\ -\frac{\sec\theta}{\sqrt{2}} & \csc 2\theta & \frac{\csc\theta}{\sqrt{2}} & \cot 2\theta \end{bmatrix} \quad (10)$$

According to the discussion around Fig. 4(b), an *N*-port device can be represented by an *N*-port *N*-node network. The topology in Fig. 2 is therefore transformed into Fig. 7, where the 180° waveguide coupler is represented by nodes 1 - 4 while the 90° waveguide coupler is by nodes 5 - 8. Between the two waveguide couplers are two fourth-order filtering couplers as introduced in Fig. 3. There are twenty-four nodes in total with eight ports. The overall 32 × 32 CM of the SPJ is shown in Fig. 8.

In the CM of the SPJ, the entries in 1 – 4 are for the 180° coupler, the entries in 5 - 9 are for the 90° coupler. The entries in 9 – 16 and 17 - 24 are for the upper and lower fourth-order filtering couplers, respectively. The remained scattered entries represent the connection between the couplers and the coupling to ports. The coupling values are also provided in Fig. 8. Note that Port 7 and Port 8 are supposed to be loaded in the real situation.

From this CM, the ideal magnitude and phase response of the filtering SPJ can be obtained. Fig. 9 and Fig. 10 show the calculated magnitude responses of the SPJ in Fig. 7 when the input signal is at Port 1 and Port 2, respectively. It can be noticed that the response has fourth-order Chebyshev characteristics. $|S_{21}|$ and $|S_{22}|$ are both - ∞ theoretically. The theoretical phase response is given in Fig. 11. It is consistent with those expressed by (1).

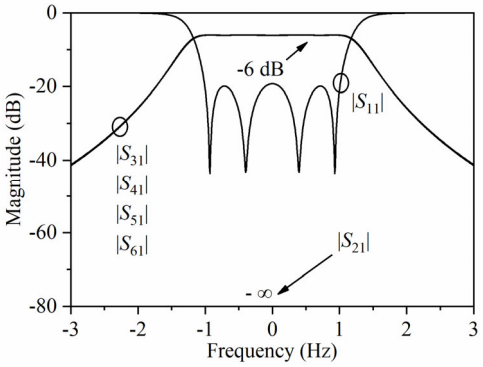

Fig. 9. Theoretical magnitude response of Port 1, from the CM of the SPJ in Fig 7.

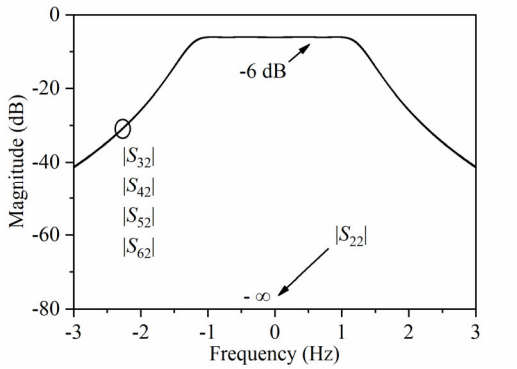

Fig. 10. Theoretical magnitude response of Port 2, from the CM of the SPJ.

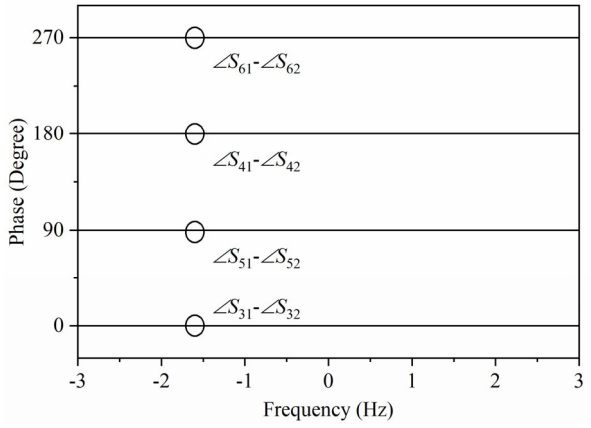

Fig. 11. Theoretical phase response of the SPJ from the CM.

IV. Realization of the Waveguide Couplers and the Hybrid CM of the SPJ

$$
\begin{cases}
m_{1,2} = -\dfrac{\sec\theta}{\sqrt{2}} \\
m_{1,3} = 0 \\
m_{1,4} = \dfrac{\sec\theta}{\sqrt{2}} \\
m_{2,3} = -\dfrac{\csc\theta}{\sqrt{2}} \\
m_{2,4} = -\csc 2\theta \\
m_{3,4} = -\dfrac{\csc\theta}{\sqrt{2}}
\end{cases}
\qquad
\begin{cases}
m_{5,6} = -\sqrt{2}\cos\theta\sec 2\theta \\
m_{5,7} = -\sec 2\theta \\
m_{5,8} = \sqrt{2}\sin\theta\sec 2\theta \\
m_{6,7} = \sqrt{2}\sin\theta\sec 2\theta \\
m_{6,8} = -\sec 2\theta \\
m_{7,8} = -\sqrt{2}\cos\theta\sec 2\theta
\end{cases}
$$

$$
\begin{cases}
m_{2,9} = m_{4,21} = m_{6,16} = m_{8,20} = 1.036 \\
m_{12,27} = m_{13,28} = m_{17,29} = m_{24,30} = 1.036 \\
m_{9,10} = m_{15,16} = m_{19,20} = m_{21,22} = 0.912 \\
m_{10,11} = m_{14,15} = m_{18,19} = m_{22,23} = 0.701 \\
m_{11,12} = m_{11,13} = m_{12,14} = m_{17,23} = m_{18,24} = m_{23,24} = 0.645 \\
m_{13,14} = m_{17,18} = -0.645 \\
m_{1,25} = m_{5,26} = m_{3,31} = m_{7,32} = 1
\end{cases}
$$

Fig. 8. Theoretical CM of the SPJ. The matrix is diagonally symmetrical.

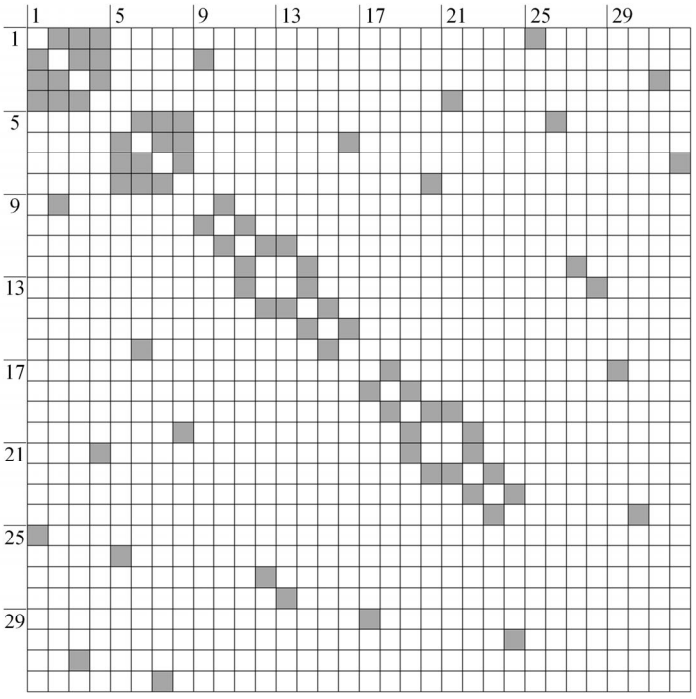

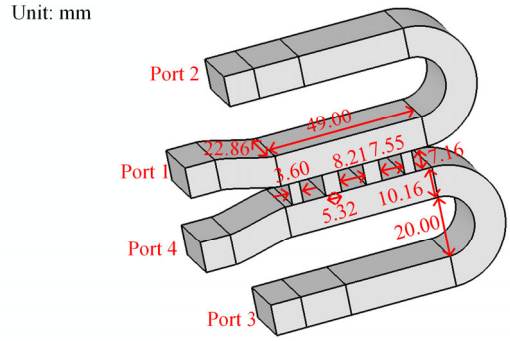

Fig. 12. 90° waveguide coupler model.

The constituent components of the SPJ can be designed separately. In this section, the two waveguide couplers will be considered first. The simulated responses of the couplers will be transferred to the corresponding part of the CM of the SPJ according to (6). This makes it possible to predict a more realistic response of the SPJ.

A. E-plane 90° waveguide coupler

A design method for multibranch waveguide couplers [22] was used here. The E-plane waveguide 90° coupler working in 9.5-10.5 GHz is shown in Fig. 12 with all the key dimensions given. The response of the 90° coupler will be given later together with that of the 180° coupler.

B. E-plane 180° waveguide coupler

The 180° waveguide coupler is built by a 90° coupler and a 90° phase shifter, as illustrated in Fig. 6(b) with the simulation model in Fig 13. The fixed phase shift is achieved by adjusting the width of the waveguides [23], shown in Fig. 13(b). The width of the waveguide connected to Port 2 is reduced to 20.16

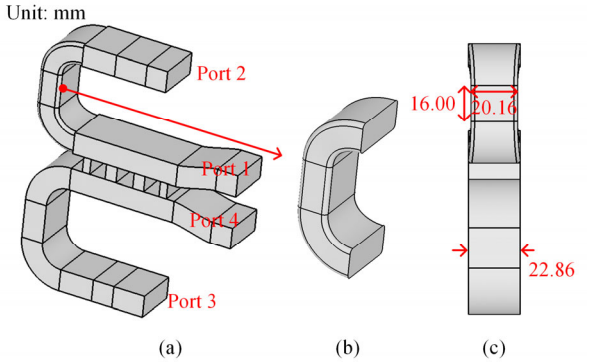

Fig. 13. 180° waveguide coupler model. (a) Overall view. (b) Enlarged view of the narrowed waveguide for phase shift purpose. (c) Side view of the coupler.

mm while the others are kept the same at 22.86 mm. The edges of the narrowed waveguide are rounded by 1 mm in radius to meet the CNC machining requirements. The narrowed waveguide provides the extra 90° phase shift.

C. Simulated responses of waveguide couplers

The simulated magnitude and phase responses of the two waveguide couplers are shown in Fig. 14. The working band of both couplers is from 9.5 to 10.5 GHz, covering the working band of the filtering coupler, which is 9.8 - 10.2 GHz. The errors of phase differences of the two couplers are less than 1°.

D. Hybrid CM of the SPJ incorporating contribution from the simulated couplers

Section III gave a method to get the CM of the SPJ involving non-resonant structures. Now that the two waveguide couplers

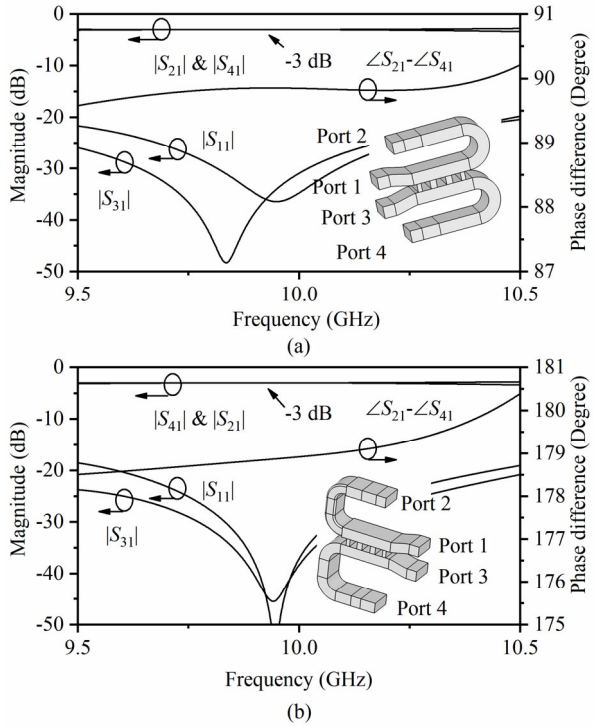

Fig. 14. Simulated magnitude and phase responses of: (a) 90° waveguide couplers and (b) 180° waveguide couplers.

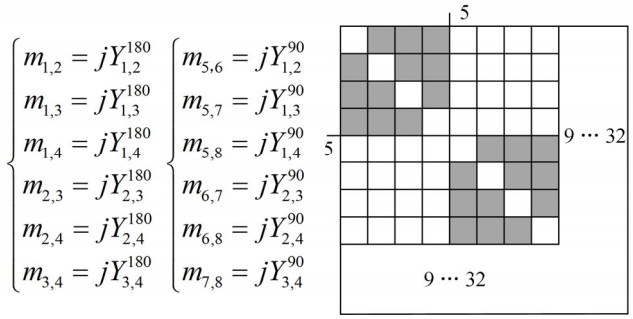

Fig. 15. CM of the SPJ combining the simulated response of the two waveguide couplers and the theoretical couplings of the two fourth-order filters.

are designed and optimized, their contribution to the whole SPJ can be incorporated into the matrix using the method described in Section III. In this way, a hybrid CM of the SPJ partly based on simulation and partly on circuit model can be constructed to predict a more realistic response.

Based on the topology shown in Fig. 7, the response in Fig. 14(a) is from node 5 - 8 while the one in Fig. 14(b) is from node 1 - 4. The simulated *S*-parameters are first transferred into *Y*-matrices [21]. A hybrid CM of the SPJ is obtained by combining the entries of the simulated *Y*-matrices, according to (6), and the theoretical couplings of the filtering coupler (in the inset of Fig. 3). The formation of this hybrid CM is illustrated in Fig. 15. $Y^{180}_{n,m}$ means the entries of the *Y*-matrix of the 180° waveguide coupler while $Y^{90}_{n,m}$ means the ones of the 90° waveguide coupler. The entries in row 9-32, column 9-32 are

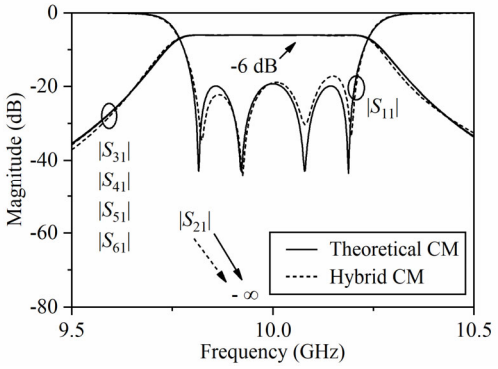

Fig. 16. Magnitude response of Port 1 from the hybrid CM of the SPJ . The response is compared with the ideal magnitude response.

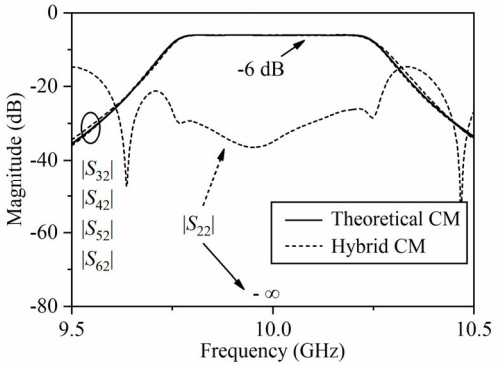

Fig. 17. Magnitude response of Port 2 from the hybrid CM of the SPJ . The response is compared with the ideal magnitude response.

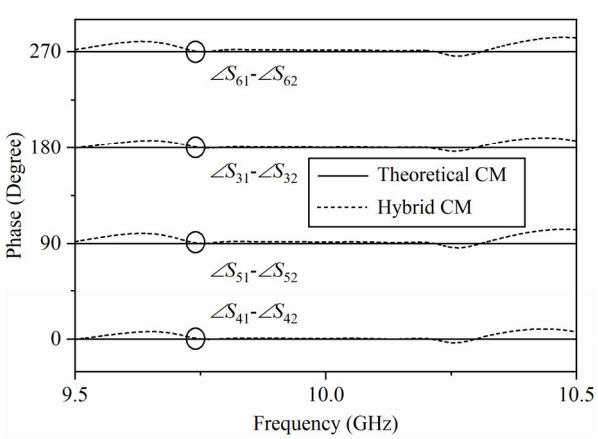

Fig. 18. Theoretical phase response of the SPJ from the hybrid CM of the SPJ.

the same as those in the CM given in Fig. 8.

Based on this hybrid CM, the responses of the SPJ in 9.5 to 10.5 GHz with two optimized waveguide couplers are derived and shown in Fig. 16-18. It can be seen $|S_{11}|$ still has the fourth-order Chebyshev response and $|S_{21}|$ is still - ∞. Ripples are shown in the $|S_{22}|$ coming from the hybrid CM. This is a result of the asymmetrical configuration brought by the two waveguide couplers.

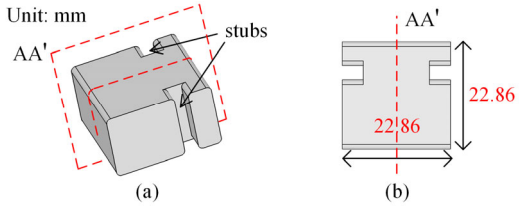

Fig. 19. Stub-loaded rectangular resonator. (a) The overall view. (b) The top view.

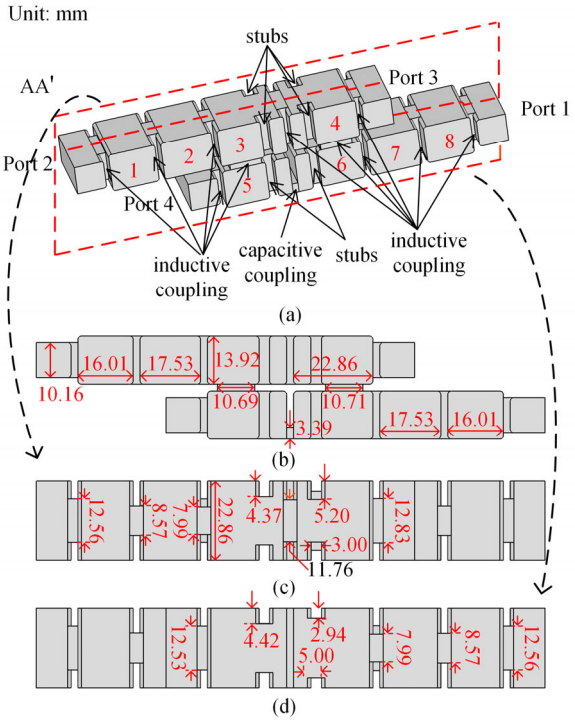

Fig. 20. The fourth-order filtering coupler and its dimensions. (a)Overall view; (b) Front view; (c) Top view; (d) Bottom view.

V. Design of the Filtering Coupler

The filtering function of this SPJ is achieved by the two identical 180° Chebyshev filtering couplers. Their bandwidth determines the bandwidth of the SPJ, which is 9.8-10.2 GHz. Fig. 19 shows the model of the stub-loaded rectangular resonator used in the filtering coupler in CST Studio Suite. The resonator is symmetric with respect to the plane AA', shown in red dashed lines. The stub pairs in different resonators have different depths to adjust the resonant frequencies. The outer dimensions of all the resonators are kept the same at 22.86 mm × 22.86 mm, as shown in Fig. 19(b). This feature eases the layout of the coupled resonators in two layers. It can keep the outer dimensions of the resonators same while adjusting the resonant frequencies. The resonators work at TE_{101} mode and plane AA' is the E plane. Fig. 20(a) shows the filtering coupler with the stub-loaded rectangular resonators. Port 1 and Port 2 are isolated from each other, as well as Port 3 and Port 4. Internal edges are rounded with 1 mm radius to meet the CNC machining requirements. Critically, the 180° phase shift is achieved by the capacitive coupling (– 90° phase shift) between resonator 5 and 6 along with the inductive couplings (+ 90° phase shift) between resonator 3 and 4, 3 and 5, 4 and 6.

The coupler is designed to have the return loss and the isolation more than 20 dB. The simulated magnitude response is shown in Fig. 21. Within the working band (9.8 - 10.2 GHz),

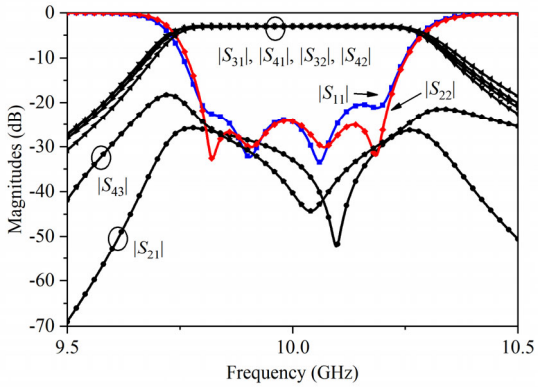

Fig. 21. Simulated S-parameters of the 180° filtering coupler in Fig. 20.

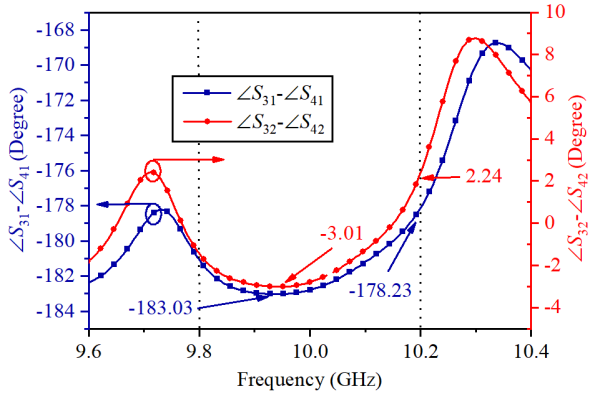

Fig. 22. Simulated phase responses of the 180° filtering coupler in Fig. 20.

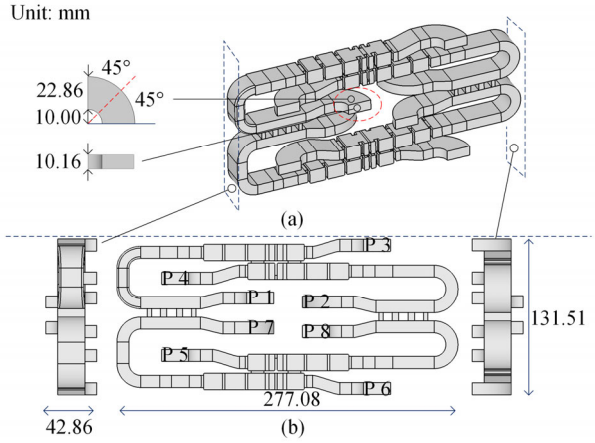

Fig. 23. SPJ air model. (a) Perspective view and waveguide bends. (b) Front view and side views of the SPJ.

the return losses and isolations all meet the specifications. The passbands are very flat and well balanced.

The simulated phase responses are shown in Fig. 22. Over the working band, $\angle S_{31}$ - $\angle S_{41}$ varies from -183.03° to -178.23°. The phase difference $\angle S_{32}$ - $\angle S_{42}$ has a maximum of 2.24° and a minimum of – 3.01°. The detailed dimensions of the coupler can be found in Fig. 20(b), (c) and (d).

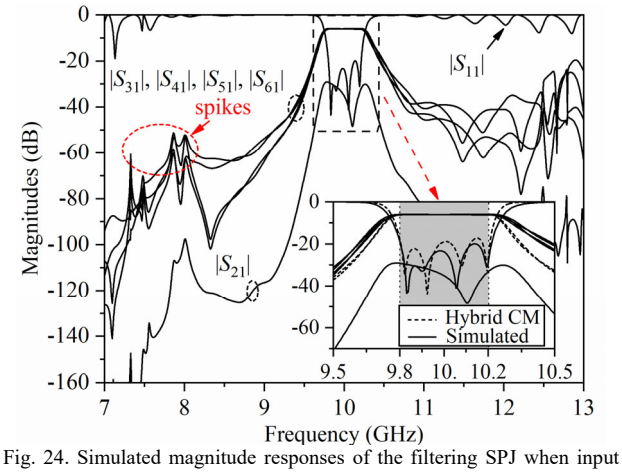

Fig. 24. Simulated magnitude responses of the filtering SPJ when input from Port 1. Inset shows the response over 9.6-10.4 GHz.

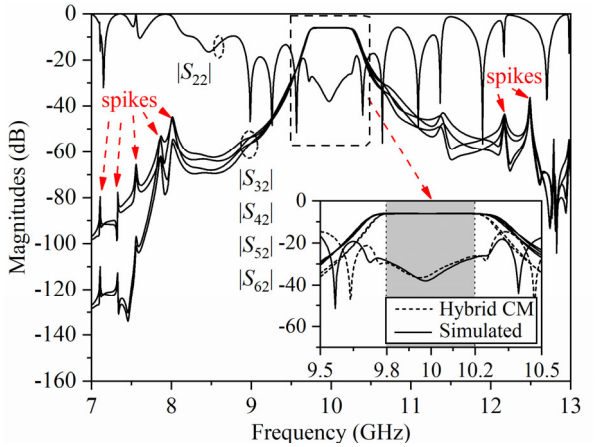

Fig. 25. Simulated magnitude responses of the filtering SPJ when input from Port 2. Inset shows the response over 9.6-10.4 GHz.

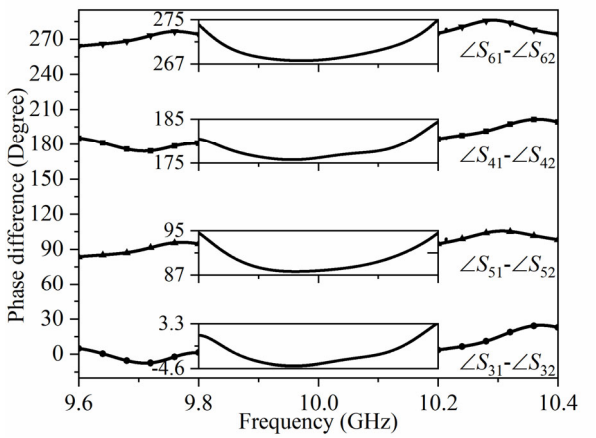

Fig. 26. Simulated phase response of the filtering SPJ from 9.6 to 10.4 GHz. The curves are zoomed over the working band (9.8 - 10.2 GHz).

VI. Design of the SPJ

Having designed all the constituent components, the E-plane-cut fourth-order filtering SPJ can now be realized. Fig. 23 shows the SPJ model in CST. In Fig. 23(a), the top and side views of a 90° bend are shown. There are eight of them to give space for flanges. The inner radius is 10.00 mm and the width of the bend is 22.86 mm. Fig. 23(b) shows the front view and side views of the SPJ. The size of the SPJ air model is 288 mm × 121 mm × 26.86 mm. P1 to P8 mark out the ports with P7 and P8 terminated with a load.

The simulated magnitude responses are shown in Fig. 24 and Fig. 25. The former is when the input is from Port 1 and the other is when input comes from Port 2. It can be seen that the transmissions have a fourth-order filtering characteristic. The insets of Fig. 24 and Fig. 25 show the magnitude responses from 9.5 to 10.5 GHz, compared with the theoretical responses from the hybrid CM. As shown in Fig. 24, the isolation between Port 1 and Port 2 is higher than 30 dB. In Fig. 25, $|S_{22}|$ is lower than -20 dB over the same operation band. $|S_{71}|$ and $|S_{82}|$ are not shown here because Port 7 and Port 8 are supposed to connect to a load. There are some spikes appearing in the response in 7-8 GHz and 12-13 GHz as pointed out. The spikes in 7-8 GHz

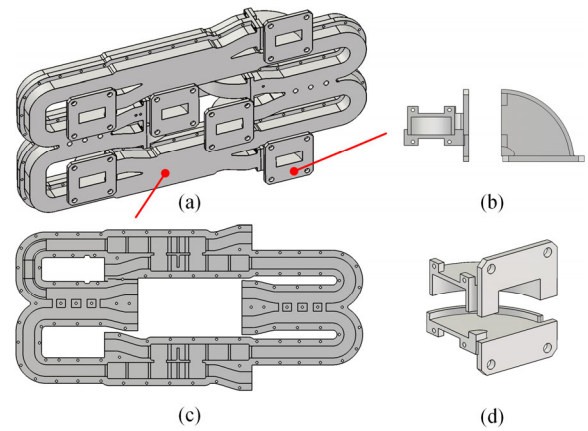

Fig. 27. Assembly of the SPJ. (a) Overall view. (b) Side and top view of the bend flange. (c) The main part of the SPJ. (d) Assembly of the bend.

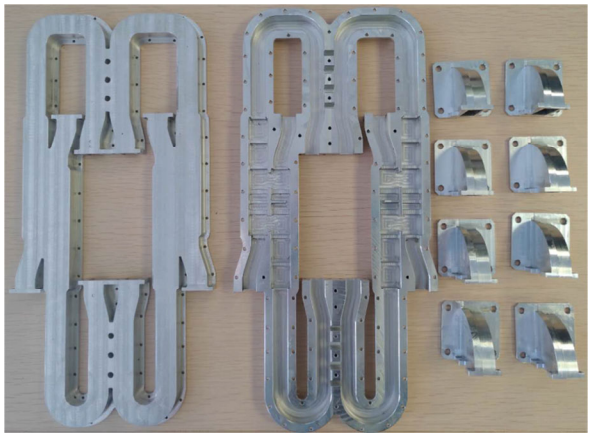

Fig. 28. The fabricated SPJ by CNC machining, shown as separate parts.

are caused by a new resonator formed by resonator 3 and 5, 4 and 6, shown in Fig. 20(a). The spikes in 12-13 GHz are the results of the higher mode in the stub-loaded resonators.

The phase responses are important in the filtering SPJ. Fig. 26 shows the simulated phase differences of the filtering SPJ from 9.6 to 10.4 GHz. The curves over the working band (9.8 to 10.2 GHz) have been enlarged to show more details. The simulated phase differences agree with those from the theory in (1). The largest phase error in simulations is 5°.

VII. Fabrication and Measurement

The SPJ was optimized and designed for fabrication using CNC machining (material: Aluminum). The metal model of the SPJ is given in Fig. 27(a). The eight identical bends, shown in Fig. 27(b), were made separately. The main part is split from the E-plane, shown in Fig. 27(c). The fabricated SPJ is shown in Fig. 28.

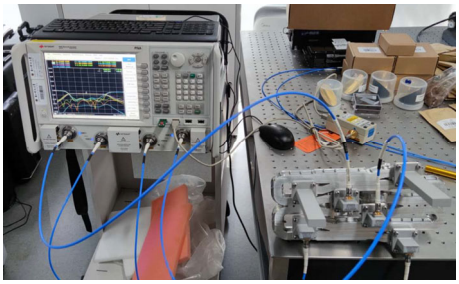

Fig. 29. Measurement setup of the SPJ.

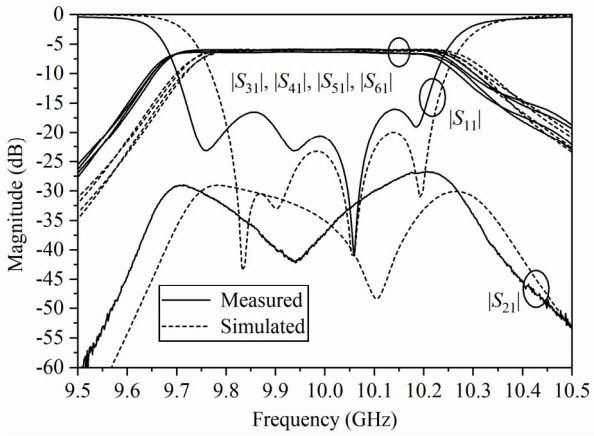

Fig. 30. Measured magnitude response of port 1 of the SPJ.

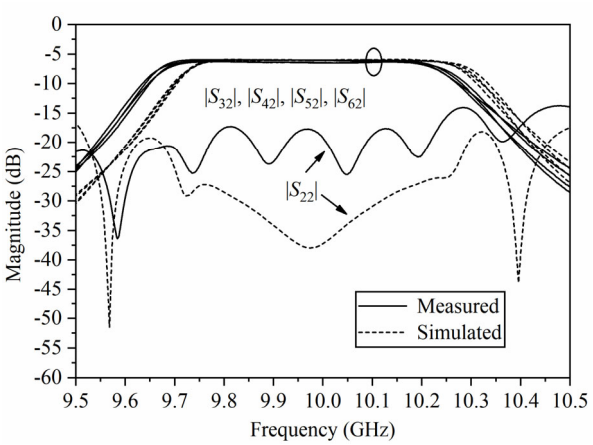

Fig. 31. Measured magnitude response from port 2 of the SPJ.

The measurement setup of the SPJ is shown in Fig. 29. There are eight ports in total and four of them are connected to loads in each measurement using a four-port vector network analyzer (N5227A). The measured magnitude response of the SPJ is shown in Fig. 30 and Fig. 31. It can be noticed that there is a small frequency shift about 0.05 GHz. The designed working band is 9.8 to 10.2 GHz while, in the measurement, this is 9.75 to 10.15 GHz. We have measured the dimensions of the fabricated model and found some dimensional errors on the order of 0.1 - 0.2 mm, which is consistent with the tolerance of the CNC machine used. Modelling shows this dimensional discrepancy, especially from the broad-wall width of the waveguide, can explain the frequency shift in the measurement.

The measured return loss at both Port 1 and 2 in the actual working band is larger than 15 dB. The insertion losses are about 6.4 dB including 6 dB power division loss in the working band with flat output magnitudes. The four reflection zeros are clearly identifiable in $|S_{11}|$ response. The phase response of the measurement, compared with the simulation, is shown in Fig. 32. The largest phase error in the measurement is 10°, which is in $\angle S_{61}$-$\angle S_{62}$ and $\angle S_{51}$-$\angle S_{52}$.

To the best of the authors' knowledge, there is only one filtering SPJ reported in the literature [13]. TABLE I compares the measured magnitude responses between this work and a few

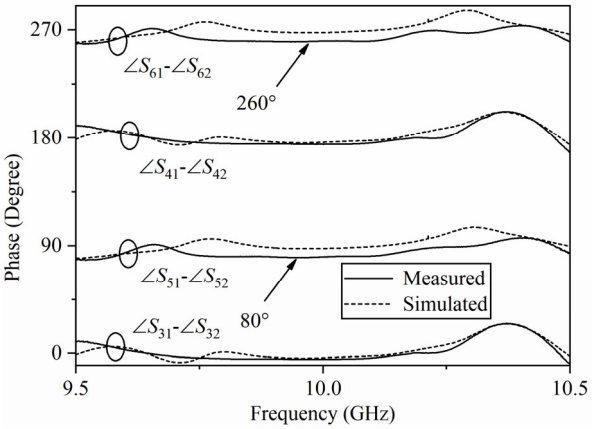

Fig. 32. Measured phase response of the SPJ.

TABLE I
COMPARISON OF MEASUREMENT RESPONSE WITH OTHER SPJS

Ref.	Return Loss* (dB)	Insertion Loss# (dB)	Magnitude Variation^ (dB)	Isolation (-|S_{21}|) (dB)	FBW/f_0& (GHz)	Filtering Function	Circuit Size (λ_g^3)
[6]	> 12.00	< 2.00	-5.00/-8.00	>18.00	20%/2.00	No	-
[7]	>15.00	< 6.50	-4.00/-12.50	>21.00	16.67%/24.00	No	-
[8]	> 10.00 / > 15.00	< 2.20	-4.30/-8.20	>17.00	6.7%/30.00	No	4.27×3.49×0.24
[13]	> 21.00	< 1.90	-6.90/-7.90	> 25.00	2.32%/7.75	Yes	-
This work	> 15.00	< 0.42	-5.90/-6.42	> 26.86	4.02%/9.95	Yes	5.87×3.18×0.84

* The worst in-band return loss of the two inputs. # The worst in-band insertion loss among the four outputs. ^The highest and lowest in-band magnitudes among the four outputs. & FBW = Fractional Bandwidth and f_0 = Center frequency.

other SPJs. It can be noticed that the return loss, insertion loss, output balance and isolation of this work are all competitive.

VII. CONCLUSION

This paper presents an E-plane filtering SPJ working at 10 GHz. A new SPJ topology based on 180° filtering couplers was proposed. To analyze the theoretical response of the SPJ, the CM of the entire SPJ, including both the non-resonant and the filtering couplers, was constructed. A comprehensive analytical approach was presented. Two identical E-plane fourth-order Chebyshev filtering couplers were designed. Stub-loaded resonators were adopted in the coupler to keep a consistent profile and ease the layout. The measurement showed a very good agreement with the simulation and verified the design approach of the filtering SPJ. A very flat passband with over 15 dB return loss was achieved with the help of the embedded resonators. A reasonably good phase performance has been achieved, considering the complex structure and multiple assembly steps. 3D printing may be used to reduce the assembly, especially around the bends at the output ports. The proven waveguide filtering SPJ concept may be used in high mm-wave designs for radar applications. Also, the waveguide SPJ can be employed in satellite systems, where high-power phenomenon such as multipactor should be considered. In our design, the favourable E-plane cut was implemented and the use of sharp corners were avoided to help with the power handling. More detailed design guideline on multipactor can be found in European Cooperation for Space Standardization [24]. The generic CM technique developed for the filtering SPJ can be applied to synthesize and analyze other complex multi-port signal distribution networks.

REFERENCES

[1] T. Hentschel, “The six-port as a communications receiver”, *IEEE Trans. Microw. Theory Tech.*, vol. 53, no. 3, pp. 1039-1047, Mar. 2005.

[2] D. Ghosh and G. Kumar, "Six-Port Reflectometer Using Edge-Coupled Microstrip Couplers," *IEEE Microw. Wireless Compon. Lett.*, vol. 27, no. 3, pp. 245-247, Mar. 2017.

[3] G. Engen and C. Hoer, “Application of an arbitrary 6-port junction to power-measurement problems”, *IEEE Trans. Instrum*. Meas., vol. IM-21, no. 4, pp. 470-474, Nov. 1972.

[4] J. Li, R. G. Bosisio and K. Wu, "Performing PSK demodulation using six-ports," *Symposium on Antenna Technology and Applied Electromagnetics [ANTEM 1994],* Ottawa, Canada, 1994, pp. 15-18.

[5] A. Koelpin, G. Vinci, B. Laemmle, D. Kissinger and R. Weigel, “The six-port in modern society”, *IEEE Microwave Mag.*, vol. 11, no. 7, pp. 35-43, Nov. 2010.

[6] S. M. Winter, A. Koelpin and R. Weigel, “Six-port receiver analog front-end: multilayer design and system simulation”, *IEEE Microwave Trans. Circuits Syst.*, vol. 55, no. 3, pp. 254-258, Mar.. 2008.

[7] Xinyu Xu, R. G. Bosisio and Ke Wu, "A new six-port junction based on substrate integrated waveguide technology," *IEEE Trans. on Microw. Theory Tech.*, vol. 53, no. 7, pp. 2267-2273, Jul. 2005.

[8] A. A. Sakr, W. M. Dyab and K. Wu, "A dually polarized six-port junction based on polarization-selective coupling for polarization-inclusive remote sensing," *IEEE Trans. on Microw. Theory Tech.*, vol. 66, no. 8, pp. 3817-3827, Aug. 2018.

[9] W. Wu, Y. Yin, S. Zuo, Z. Zhang and J. Xie, "A new compact filter-antenna for modern wireless communication systems," *IEEE Antennas Wireless Propag. Lett.*, vol. 10, pp. 1131-1134, 2011.

[10] K.-X. Wang, X. Y. Zhang, S. Y. Zheng, and Q. Xue, “Compact filtering rat-race hybrid with wide stopband,” *IEEE Trans. Microw. Theory Techn.*, vol. 63, no. 8, pp. 2550–2560, Aug. 2015.

[11] Q. Shao, F. Chen, Y. Wang, Q. Chu, M. J. Lancaster, “Design of Modified 4×6 Filtering Butler Matrix Based on All-Resonator Structures”, *IEEE Trans. Microw. Theo. Techn.*, vol. 67, no. 9, pp. 3617-3627, Sep. 2019.

[12] G. Vinci, A. Koelpin, F. Barbon and R. Weigel, "Six-port-based direction-of-arrival detection system," *2010 Asia-Pacific Microwave Conference, Yokohama*, 2010, pp. 1817-1820.

[13] Y. J. Cheng and Y. Fan, “Compact substrate-integrated waveguide bandpass rat-race coupler and its microwave applications,” *IET Microw. Antennas Propag.*, vol. 6, pp. 1000–1006, Sep. 2012.

[14] R. J. Cameron, "Advanced coupling matrix synthesis techniques for microwave filters," IEEE Trans. Microw. Theo. Techn., vol. 51, no. 1, pp. 1-10, Jan. 2003.

[15] Y. C. Li, K. C. Wu, and Q. Xue, “Power amplifier integrated with bandpass filter for long term evolution application,” *IEEE Microw. Wireless Compon. Lett.*, vol. 23, no. 8, pp. 424–426, Aug. 2013.

[16] Y.-S. Lin, J.-F. Wu, W.-F. Hsia, P.-C. Wang, and Y.-H. Chung, “Design of electronically switchable single-to-balanced bandpass low-noise amplifier,” *IET Microw. Antennas Propag*., vol. 7, no. 7, pp. 510–517, May 2013.

[17] Y. Gao, J. Powell, X. Shang and M. J. Lancaster, "Coupling Matrix-Based Design of Waveguide Filter Amplifiers," *IEEE Trans. Microw. Theo. Techn.,* vol. 66, no. 12, pp. 5300-5309, Dec. 2018.

[18] Y. Gao, X. Shang, C. Guo, J. Powell, Y. Wang, and M. J. Lancaster, “Integrated waveguide filter amplifier using the coupling matrix technique,” IEEE Microw. Wireless Compon. Lett., vol. 29, no. 4, pp. 267–269, Apr. 2019.

[19] Yang Gao, Fan Zhang, Xin Lv, Cheng Guo, Xiaobang Shang, Yi Wang, Jiashan Liu, Yuhuai Liu, Juin J. Liou, Michael J. Lancaster, “Substrate integrated waveguide filter amplifier design using active coupling matrix technique”, *IEEE Trans. Microw. Theo. Techn.*, vol. 68, no. 5, pp. 1706-1716, May 2020.

[20] G.L. Matthaei, L. Young, E.M.T. Jones, “Microwave filters, impedance-matching networks, and coupling structures,” McGrawHill, New York, NY, USA, 1964.

[21] Pozar, D. M, “Microwave engineering,” Hoboken, NJ: J. Wiley.

[22] K. G. Patterson, "A Method for Accurate Design of a Broad-Band Multibranch Waveguide Coupler," in IRE Transactions on Microwave Theory and Techniques, vol. 7, no. 4, pp. 466-473, Oct. 1959.

[23] Y. Cheng, W. Hong and K. Wu, "Novel substrate integrated waveguide fixed phase shifter for 180-degree directional coupler," *2007 IEEE/MTT-S International Microwave Symposium,* Honolulu, HI, 2007, pp. 189-192.

[24] ECSS Secretariat, "Multipactor design and test," ESA-ESTEC Requirements & Standards Division, Noordwijk, The Netherlands, ESA-ESTEC, Tech. Rep. ECSS-E-ST-20-01C, 2020.

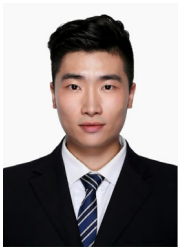

Xun Chen was born in Chengdu, China. He received the B.Eng. and M.Eng. degree from University of Electronic Science and Technology of China, China, in 2015 and 2018, respectively. He is currently working toward the Ph.D. degree at University of Birmingham, UK and Southern University of Science and Technology, China. His research focuses on coupling matrix and passive devices, including diplexers, couplers and six-port junctions.

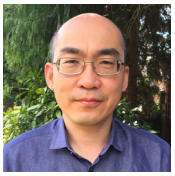

Yi Wang (M'09–SM'12) was born in Shandong, China. He received the B.Sc. degree in applied physics and M.Sc. degree in condensed matter physics from the University of Science and Technology, Beijing, China, in 1998 and 2001, respectively, and the Ph.D. degree in electronic and electrical engineering from the University of Birmingham, Edgbaston, Birmingham, U.K., in 2005.

From 2004 to 2011, he was a Research Fellow at the University of Birmingham. In 2011, he became a Senior Lecturer and then Reader at the University of Greenwich, U.K.. He is currently an Associate Professor with the University of Birmingham. He is the author of over 170 research papers. He has been the reviewer of several major microwave, antenna and sensor journals and an Associate Editor of IET MAP. He serves the TPC Chair of 2021 European Microwave Conference. His current research interests include multiport filtering networks, filter-antenna integration, millimeter-wave and terahertz antennas and devices for metrology, communication, and sensing. He is particularly interested in working with new materials and various novel manufacturing techniques, such as micromachining and 3D printing, for RF/microwave applications.

Talal Skaik received the M.Sc. degree in communications engineering and the Ph.D. degree in microwave engineering from the University of Birmingham, Birmingham, U.K., in 2007 and 2011, respectively.

In 2011, he joined the electrical engineering department at the Islamic University of Gaza, Palestine, as an assistant professor then was promoted to an associate professor in 2018. He is currently working as a research fellow with the University of Birmingham. His research interests include microwave filters and antennas, 3D-printed microwave devices, temperature compensated filters for satellite payloads, multi-port coupled resonator structures and energy harvesting circuits.

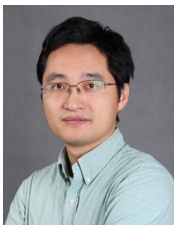

Qingfeng Zhang (Senior Member, IEEE) received the B.E. degree in electrical engineering from the University of Science and Technology of China (USTC), Hefei, China, in 2007, and the Ph.D. degree in electrical engineering from Nanyang Technological University, Singapore, in 2011.

From June 2011 to December 2013, he was a Post-Doctoral Fellow with the Poly-Grames Research Center, École Polytechnique de Montréal, Montreal, QC, Canada. Since December 2013, he has been with Southern University of Science and Technology (SUSTech), Shenzhen, China, where he is currently an Associate Professor with tenure. His research interests are largely in emerging novel electromagnetics technologies in which he has a special interest in dispersion engineering at microwave and millimeter-wave frequencies.

Dr. Zhang has served as a TPC member for various international conferences and on the review board of numerous journals in electromagnetics. He is also a fellow of the Institution of Engineering and Technology (IET). He received the URSI Young Scientist Award and the ACES Young Scientist Award in 2018. He is also the Vice-Chair of the IEEE Antennas and Propagation Society Shenzhen Chapter. He was the Publication Chair of the 2016 IEEE International Conference on Communication Systems (ICCS), the Local Organization Committee Co-Chair of 2017 IEEE Electrical Design of Advanced Packaging and Systems (EDAPS) Symposium, the TPC Co-Chair of Track 9 (Passive ICs and Active Antennas) in 2018 IEEE International Conference on Integrated Circuits, Technologies and Applications (ICTA), and the Track Chair of 2019 ComComAp. He has served as a Lead Guest Editor for the *International Journal of Antennas and Propagation* from 2014 to 2015. He has been serving as an Associate Editor for IEEE ACCESS since 2017.